Scripta Materialia 256 (2025) 116434

Contents lists available at ScienceDirect

Scripta Materialia

journal homepage: www.journals.elsevier.com/scripta-materialia

3D micromechanical interaction of thin-film retained austenite and lath martensite by computational plasticity

Tim Fischer [a,b,*], Mina Amiri [a], Joshua Kumpati [a], Peter Hedström [a], Annika Borgenstam [a]

[a] Department of Materials Science and Engineering, KTH Royal Institute of Technology, Brinellvägen 23, Stockholm, SE-10044, Sweden
[b] Institute of Materials Physics and Technology, Hamburg University of Technology, Eißendorfer Straße 42, Hamburg, D-21073, Germany

ARTICLE INFO

Keywords:
Martensite
Retained austenite
Advanced high-strength steels
Micromechanics
Microstructure

ABSTRACT

To exploit the full potential of advanced high-strength steels (AHSS), a more in-depth understanding of the complex micromechanical interaction of thin-film retained austenite (RA) and lath martensite is indispensable. Inspired by the medium-Mn steel microstructure, a three-dimensional micromechanical modeling approach is therefore proposed in the present work, embedding the thin RA films explicitly into the hierarchical lath martensite structure. This enables systematic studies of the effect of RA film thickness and volume fraction on the local stresses and strains as well as their partitioning within the microstructure. The investigations reveal that with shrinking RA volume fraction, both stress and especially strain heterogeneity in the thin-film RA intensifies. In the martensite blocks, stress and strain heterogeneity also intensifies, although stresses are generally more heterogeneously, and strains much more homogeneously, distributed than in RA. The results underline the key role of RA with thin-film morphology for further optimizing AHSS microstructures.

Medium-Mn steels as part of the 3rd generation advanced high-strength steels (AHSS) enjoy considerable attention in recent times [1,2]. This attention is largely driven by their higher strength, greater formability and lower cost compared to the high-Mn predecessors, i.e. twinning-induced plasticity (TWIP) steels [2]. The emerging class of medium-Mn steels is distinguished by a significant amount of retained austenite (RA), incorporated for example in a hierarchical lath martensite matrix, forming a characteristic two-phase microstructure [3,4]. The RA provides enhanced ductility due to a higher strain hardening rate triggered by the transformation-induced plasticity (TRIP) effect after forming martensite [1]. While lath martensite has a specific hierarchical structure with prior austenite grain (PAG) structure, packets, (sub-)blocks and laths of particular crystallography [5–20], the RA morphology is either thin-film or blocky depending on the processing conditions [3]. Experimental observations indicate that the mechanical stability of the thin RA films is typically higher than of the block morphology [21,22]. However, the influence of morphology remains a topic of debate, and the exact role of morphology is still not entirely clear. Other factors, such as composition, size and surrounding matrix or different local stresses in these two morphology variants, may also play a role [3].

To guide the microstructure-based development of AHSS, the present work seeks to computationally unveil the complex micromechanical interaction of thin-film RA and lath martensite using full-field crystal plasticity simulations. Full-field simulations are chosen as the complex micromechanical interaction cannot be readily captured by phenomenological or empirical models [23–26]. The in-depth micromechanical analysis of the interaction between the two microstructural constituents also provides valuable new insights into the overall RA stability behavior. At this point, it is important to recall that the role of interlath RA films has been previously studied using crystal plasticity simulations, with a focus on the damage initiation behavior in both dual-phase [27–30] and fully martensitic microstructures [31,32]. However, in those computational studies, the thin RA films were not explicitly embedded in the lath martensite structure in a three-dimensional (3D) setting. The present work attempts to fill this knowledge gap by systematically examining the impact of RA layer thickness, and consequently its volume fraction, on local stresses and strains. Future work will aim to explore both features independently. In this context, stress

* Corresponding author at: Department of Materials Science and Engineering, KTH Royal Institute of Technology, Brinellvägen 23, Stockholm, SE-10044, Sweden.
E-mail address: timfis@kth.se (T. Fischer).

https://doi.org/10.1016/j.scriptamat.2024.116434
Received 20 August 2024; Received in revised form 10 October 2024; Accepted 24 October 2024
Available online 30 October 2024

Table 1
Chemical composition in wt.% and microstructural constituents of the investigated medium-Mn steel, comprising lath martensite (matrix) and thin-film retained austenite (RA).

C	Mn	Fe	Two-phase microstructure
0.18	5.08	bal.	lath martensite + thin-film RA

and strain partitioning within the microstructure is also of particular interest [33–35].

The material investigated is a medium-Mn steel, whose chemical composition is detailed in Table 1. Different heat treatment cycles are conducted to attain the desired two-phase microstructure of a lath martensite matrix and RA with a distinct thin-film morphology. All samples are cut from an 8 mm thick hot-rolled steel plate. Throughout the heat treatment, the samples are encapsulated in quartz tubes to prevent oxidation by the surrounding atmosphere. The entire heat treatment process is summarized in [3]. In the first cycle, the material is homogenized at 1200 °C for 15 h and water quenched to room temperature (RT). In the second cycle, the steel is austenitized at 900 °C for 15 min before quenching to RT to produce a fully martensitic microstructure. Finally, in the third and final cycle, the material is intercritically annealed at 650 °C for 3 h to establish a two-phase microstructure of a martensitic matrix and RA, before water quenching to RT.

After the controlled heat treatment, the microstructure is characterized using electron backscatter diffraction (EBSD) in a JEOL-7800F scanning electron microscope (SEM). Sample preparation involved mechanical grinding and polishing to a 1 μm finish, followed by colloidal silica suspension polishing (0.02 μm) and final electropolishing for optimal surface quality. EBSD data is post-processed using the capabilities of the open-source software MTEX [36,37]. The evaluation of the reconstructed PAGs is based on the single-step version of the variant graph algorithm, including the determination of a representative orientation relationship as described in [38]. This representative orientation relationship is crucial for successful reconstruction, rather than considering only the austenite-to-martensite Kurdjumov–Sachs (KS) orientation relationship and the crystallographic orientation of each martensite variant [38,39]. Closely related orientation relationships (misorientation angle about 2.5°), such as Nishiyama–Wassermann [40] and Greninger–Troiano [41], present alternatives, where only minor changes in the micromechanical response are anticipated between the different relationships. It is noted that the reconstruction quality may be affected by the intercritical annealing at 650 °C, which could introduce minor changes to the orientation map from its original martensitic state.

Fig. 1 shows the EBSD characterization of the medium-Mn steel revealing the initial two-phase microstructure, comprising RA as well as lath martensite (M). The individual, clearly defined microstructural constituents are indicated by the color-coded phase (*top*) and inverse pole figure (IPF) maps (*bottom*). The RA volume fraction is about 33%. Also, a reconstructed, fairly large PAG size is revealed from the IPF map (*bottom right*). While RA unfolds the characteristic thin-film morphology, the lath martensite structure exhibits a typical packet and block-like character. The thin RA films are embedded between the martensite blocks and laths, with the film thickness being visibly smaller than the block width. The average aspect ratios measured are 2.9±1.7 for the RA films and 2.7±1.6 for the martensite blocks. Regarding the corresponding average long axis, the RA films exhibit values of 0.50±0.46 μm, while the martensite blocks show values of 0.69±0.96 μm. Within a packet, both the films and blocks are arranged nearly parallel, although films and blocks can be partially interrupted. The IPF maps also clearly show that the crystallographic orientation of the RA films deviates from that of the martensite blocks. Within a single PAG, the RA films exhibit a uniform orientation, whereas the martensite blocks adopt varying orientations following the KS orientation relationship.

Fig. 2 illustrates the synthetically generated two-phase microstructures employed for the computational study based on color-coded phase maps (*top and middle*) for three selected RA volume fractions of 33, 23 and 8%. It is worth noting that synthetically generated structures, in contrast to real measured microstructure representations, play a decisive role in materials design due to their highly flexible setup [23,42]. The three different volume fractions are derived from a systematic variation of the ratio of RA thin-film thickness to martensite block width amounting to 1:2 (33%), 3:10 (23%) and 1:10 (8%). While thinning the RA thin-film thickness, the block width is kept constant and one RA film is always located between two blocks. For each RA volume fraction, however, both the block width and thin-film thickness are assumed to remain the same and do not vary within the synthetic microstructure [43,44]. As sub-blocks and laths within a block form substructure units with low misorientation angle and their strength contribution is smaller and therefore often neglected, blocks (and thin-films) provide the bottom scale in the present modeling approach [45,46]. In general, the synthetic microstructures for each volume fraction are generated according to the principle of replicating the martensitic transformation process (starting from the top scale):

1. Fully austenitic microstructure (representing the PAG scale) composed of equiaxed grains with random crystallographic orientation.
2. Intermediate martensitic microstructure (representing the packet scale) consisting of equiaxed sub-grains (packets) with random selection of one of the four possible habit planes.
3. Two-phase martensitic/austenitic microstructure (representing the block/RA scale) comprising parallel sub-packet lamellae (blocks/RA) stacked in the habit plane normal direction, with one of the six possible martensite variants randomly selected for each of the four planes.

In total 24 variants (six variants for each of the four possible habit planes) are available [39]. Instead of selecting one of the variants according to the KS relationship, the thin RA films are assigned their crystallographic orientation based on the random assignment for the top PAG scale. The resulting underlying orientation situation is also illustrated in Fig. 2 (*bottom*) utilizing IPF maps. Further details on the synthetic generation of the pure lath martensite structure can be found in [45,47]. To accurately represent the two-phase microstructure, experimentally measured sizes of microstructural constituents are supplied as input into the multiscale tessellation method available in the open-source software Neper [48]. Based on the investigations by [12], the relationship between packet and PAG size for numerous different martensitic steels is given by $d_p = 0.400 \cdot d_g$, where d_p is the average packet size and d_g the average PAG size. By initially assuming three PAGs in the synthetic microstructure for the different RA volume fractions, the validity of this relationship is ensured by adjusting the number of packets (27 in total) accordingly. A similar relationship holds for the block width specified by $w_b = 0.067 \cdot d_g$, where w_b is the average block width [12]. Again, the number of blocks or rather their width is varied until the validity of the relationship is fulfilled. With a RA volume fraction of 33%, this yields 299 blocks and films, with a volume fraction of 23% the number increases to 339 and with 8% to 395. Unlike in [12], each packet is not divided into six lath structures with a common orientation. For the microstructure measured here, the ratio of block width to PAG size is determined to be 0.013, which is the same order of magnitude as the value provided in [12]. It should be emphasized that selecting the size of the synthetic microstructure involves a trade-off between computational effort and the need to equally represent three different RA volume fractions.

The crystal plasticity finite element method (CPFEM) is exploited to systematically investigate the intrinsic effect of thin-film RA volume fraction on the mechanical response at the microscopic scale. To separate the components of elastic $\mathbf{F}_e$ and plastic deformation $\mathbf{F}_p$ in this approach, a multiplicative decomposition of the deformation gradient

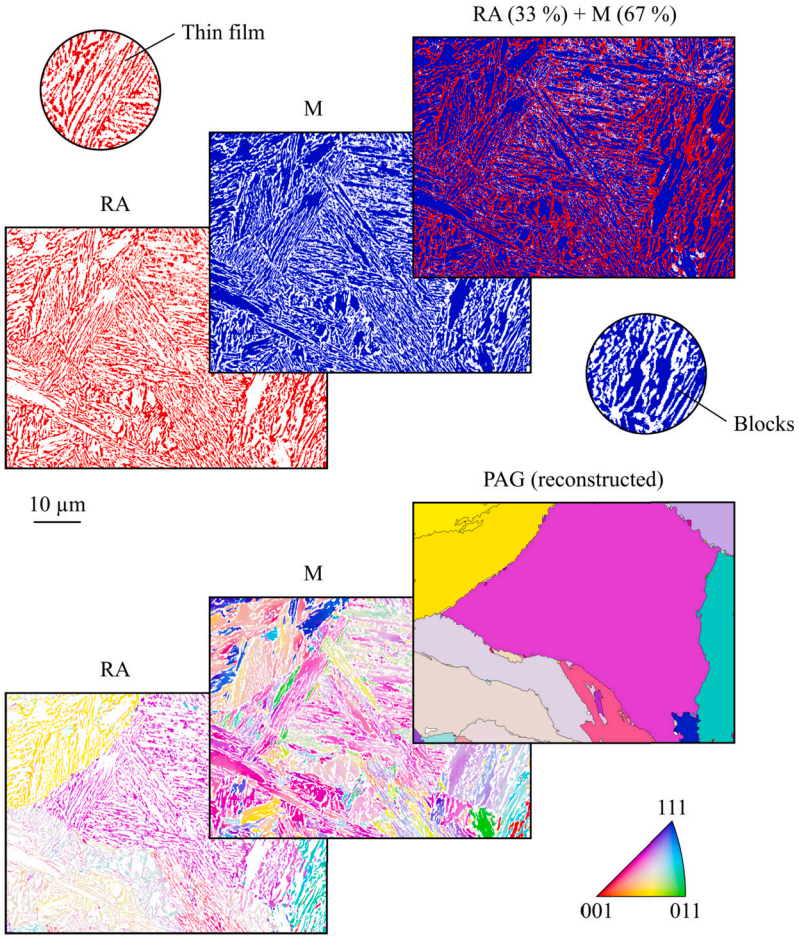

Fig. 1. EBSD characterization of the medium-Mn steel revealing a two-phase microstructure, encompassing thin-film retained austenite (RA) as well as block-like lath martensite (M). The individual microstructural constituents are highlighted by color-coded phase (*top*) and inverse pole figure (IPF) maps (*bottom*). Based on the color-coded phase maps, a RA volume fraction of about 33% can be ascertained. A reconstructed, fairly large prior austenite grain (PAG) size is evident from the IPF map. (For interpretation of the colors in the figure(s), the reader is referred to the web version of this article.)

by $\mathbf{F} = \mathbf{F}_e\mathbf{F}_p$ is executed. The generalized Hooke's law with $\mathbf{S} = \mathbb{C} : \mathbf{E}$ is employed to find the actual stress state in the material. This relates the elastic Green–Lagrange strain $\mathbf{E}$ with the second Piola–Kirchhoff stress $\mathbf{S}$ through the elastic stiffness $\mathbb{C}$. Given the identity tensor $\mathbf{I}$, the Green-Lagrange strain is calculated from $\mathbf{E} = 1/2\left(\mathbf{F}_e^{\mathrm{T}}\mathbf{F}_e - \mathbf{I}\right)$. The elastic stiffness inherits the symmetrical properties of the underlying crystal lattice, whereby only three elastic constants (C_{11}, C_{12} and C_{44}) are relevant due to this symmetry. The dislocation slip-induced plastic component is derived from the plastic velocity gradient $\mathbf{L}_p$. Here, the actual crystal plasticity sets in by establishing the sum of the slip rate $\dot{\gamma}^{\alpha}$ over the total number of slip systems N_s

$$\mathbf{L}_p = \dot{\mathbf{F}}_p\mathbf{F}_p^{-1} = \sum_{\alpha=1}^{N_s} \dot{\gamma}^{\alpha}\, \mathbf{m}^{\alpha} \otimes \mathbf{n}^{\alpha}\,, \tag{1}$$

where $\mathbf{m}^{\alpha}$ is the slip direction and $\mathbf{n}^{\alpha}$ the slip plane normal of a slip system α [49].

To qualify the material hardening, a phenomenological description is deployed. On each slip system, the shear rate progresses according to the power law proposed by [50–52]

$$\dot{\gamma}^{\alpha} = \dot{\gamma}_0 \left|\frac{\tau^{\alpha}}{s^{\alpha}}\right|^{\frac{1}{m}} \mathrm{sgn}\left(\tau^{\alpha}\right)\,, \tag{2}$$

where $\dot{\gamma}_0$ is the reference shear rate and τ^{α} the resolved shear stress opposed to the critical resolved shear stress s^{α} (CRSS). Strain rate sensitivity is reflected by the material parameter m. How the slip system β affects the hardening behavior of system α is mirrored in the CRSS evolution by

$$\dot{s}^{\alpha} = \sum_{\beta=1}^{N_s} h_{\alpha\beta} \left|\dot{\gamma}^{\beta}\right|\,, \tag{3}$$

where $h_{\alpha\beta}$ is the interaction hardening matrix

$$h_{\alpha\beta} = q_{\alpha\beta}\left[h_0\left(1 - \frac{s^{\beta}}{s_{\infty}}\right)^{n}\right]\,, \tag{4}$$

determining the micromechanical interaction between the different systems through the slip-slip matrix $q_{\alpha\beta}$ (1.0 for coplanar slip systems and 1.4 otherwise). For all slip systems, the slip hardening parameters h_0, n and s_{∞} are identical. To integrate the constitutive law outlined above over time, the CPFEM model is implemented in the commercial finite element (FE) software Abaqus using a customized material subroutine [42]. The elastic constants and crystal plasticity parameters for the face-centered cubic (fcc) thin-film RA and body-centered cubic (bcc) blocky martensite are listed in Table 2. The parameters listed are based on the extensive work of Maresca et al. [31,28,29], initially determined from experimental microtensile test data reported in [53]. It is important to note that different RA volume fractions affect the carbon content in RA and thus its mechanical properties [3]. However, since the present study concerns only the morphological aspects, this influence is overlooked and the parameters assumed are identical for all three volume fractions.

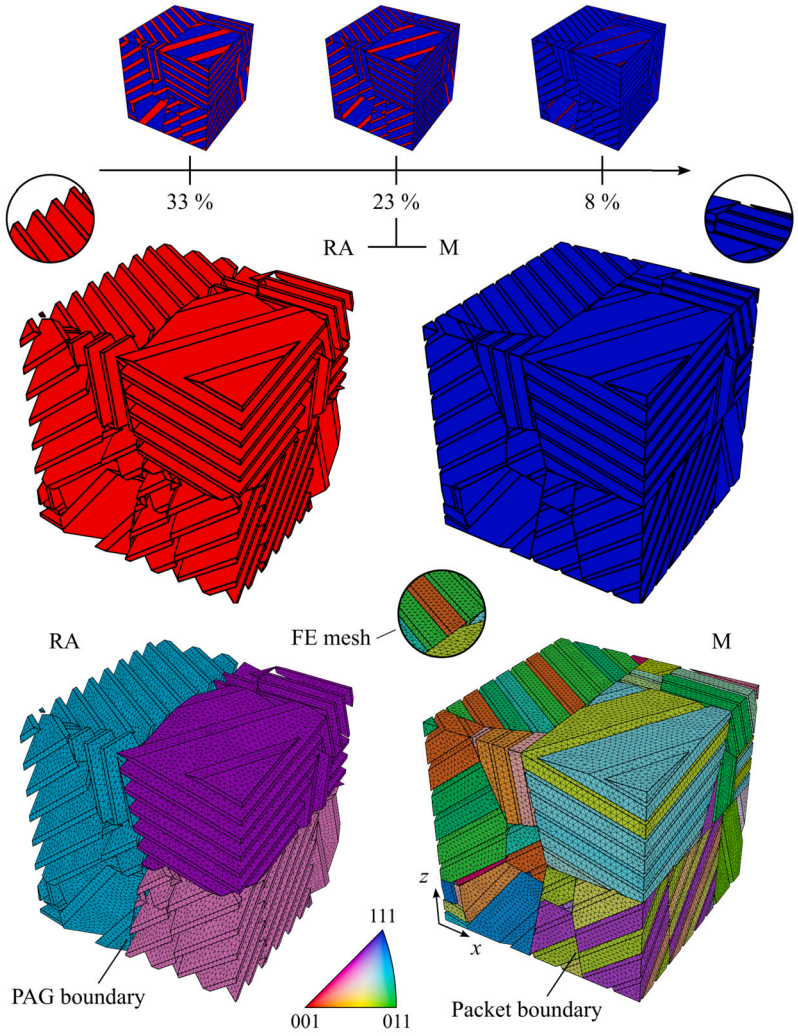

Fig. 2. Representative two-phase medium-Mn steel microstructures. The thickness of the thin-film retained austenite (RA) is systematically thinned, while the width of the martensite (M) blocks remain constant, reducing the RA volume fraction (*top*). Based on the corresponding finite element (FE) models (*bottom*), the underlying crystallographic orientations emerge. The thin RA films display a uniform orientation within a single prior austenite grain (PAG), while the orientations of the M blocks adhere to the Kurdjumov–Sachs relationship.

Table 2
Elastic constants and crystal plasticity parameters of thin-film retained austenite (RA) as well as block-like lath martensite (M) [31,28,29]. Plastic deformation of thin-film RA occurs on the 12 octahedral face-centered cubic (fcc) slip systems $\{111\}\langle 110\rangle$. In contrast, plastic deformation of block-type M is considered on the 12 primary and 12 secondary body-centered cubic (bcc) slip systems $\{110\}\langle 111\rangle$ and $\{112\}\langle 111\rangle$ respectively.

Property	Value	Unit	Property	Value	Unit
Thin-film RA (fcc)			Block-like M (bcc)		
C_{11}	268	GPa	C_{11}	349	GPa
C_{12}	156	GPa	C_{12}	202	GPa
C_{44}	136	GPa	C_{44}	176	GPa
$\dot{\gamma}_0$	0.01	1/s	$\dot{\gamma}_0$	0.01	1/s
s_0	265	MPa	s_0	765	MPa
s_∞	340	MPa	s_∞	3000	MPa
h_0	250	MPa	h_0	2250	MPa
m	0.05	-	m	0.05	-
n	1.5	-	n	1.5	-

Due to the different RA volume fractions investigated, varying mesh densities are required to accurately discretize the two-phase microstructure representations (Fig. 2, *bottom*). For example, with an RA volume fraction of 33%, the microstructure representation is meshed using 611,000 tetrahedral elements with linear shape functions and full integration. In contrast, with an RA volume fraction of 8%, the number of elements rises to around 1,013,000. The unstructured meshing method with tetrahedral elements is favored as it allows precise mapping of stresses and strains at the boundaries. This is in contrast to the structured meshing method, based on hexahedral elements or Fast Fourier Transform (FFT) calculations using voxels [42,54]. For achieving a uniaxial stress state, corresponding in most cases to experimental tensile test conditions, minimum boundary conditions are imposed [55,56]. To this end, the top face is axially displaced in z-direction under quasi-static loading until a macroscopic tensile strain of 3% is attained (see FE model in Fig. 2, *bottom*). The opposite bottom face is fixed in the axial direction. To prevent rigid body motion, two vertices on the bottom face are additionally fixed. All four lateral faces remain free to accommodate contraction perpendicular to the loading direction.

For qualitative assessment, Fig. 3 shows the predicted equivalent stress (*top*) and strain contour plots (*middle*) at 0.3% macroscopic deformation as a function of thin-film RA volume fraction (*left to right*). In the case of 23% RA volume fraction, locations of severe stress concentration and strain localization within the two-phase microstructure at 1.5% macroscopic deformation are indicated by arrows (*bottom*). For reference, PAG boundaries are also highlighted. A characteristic hetero-

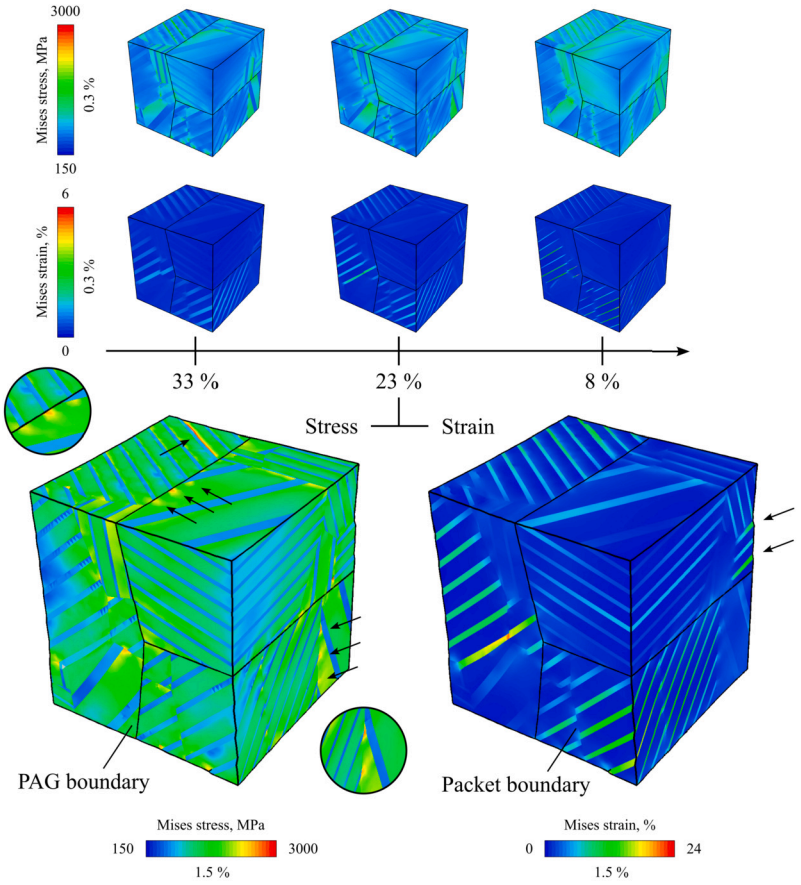

Fig. 3. Predicted equivalent stress (*top*) and strain contour plots (*middle*) at 0.3% macroscopic deformation as a function of thin-film retained austenite volume fraction (*left to right*). Locations of severe stress concentration and strain localization within the two-phase microstructure representations at 1.5% macroscopic deformation are indicated by arrows (*bottom*). For reference, prior austenite grain (PAG) boundaries are highlighted.

geneous distribution of high and low values can be determined for the stresses. The higher stress values are attributed to the stronger martensite blocks and the lower ones to the softer, more ductile thin RA films. With falling RA volume fraction, the overall stress level within the two-phase microstructure appears to increase moderately. No obvious alteration can be recognized for the stress heterogeneity. What is obvious, however, is the concentration of stresses at the adjacent boundaries, i.e. PAG, packets and blocks, that accompanies increasing macroscopic deformation. This often manifests itself in characteristic stress concentration patterns arising from the sliding of the martensite blocks on the RA films (see pair of three arrows in Fig. 3, *bottom left*). Concerning the predicted strains, a distribution of high and low values is also observed, whereby the strains in the martensite blocks appear more homogeneous. As the RA volume fraction decreases, the overall strain level appears to be slightly elevated. In contrast to the stress concentrations, less distinct patterns emerge for the strain localization with increasing macroscopic deformation. However, a certain localization can be noticed at the packet boundaries. The sliding of the martensite blocks on the thin RA layers is also evident here at the edge of the analyzed microstructure domain (see arrow pair in Fig. 3, *bottom right*).

Fig. 4 provides a more quantitative assessment of the equivalent stress (*top*) and strain heterogeneities (*bottom*) at 0.3% macroscopic deformation for the different RA volume fractions using the associated statistical data. To elucidate the data trends of RA (*left*) and lath martensite with its block-like morphology (*right*), normal distribution functions (solid lines) are fitted to the computed statistics (dots). The three insets in the corners enlarge the right-hand distribution tails to emphasize extreme values. For the predicted RA distributions, it is evident due to the distribution flattening that as the volume fraction shrinks, both the heterogeneity of the stresses and, above all, that of the strains increase significantly. In the case of strains, the distribution curves are almost completely flattened. At the lowest RA volume fraction of 8%, maximum strains of over 80% are achieved. Maximum stresses emerge at the lowest RA volume fraction of 8% and arrive at values slightly above 3000 MPa. The stress and strain heterogeneity in the blocky martensite also appears to be dependent on the RA volume fraction, albeit less obviously. What is obvious, however, is that compared to the thin RA films, the stresses in the martensite are distributed much more heterogeneously at a higher level, likely due to its enhanced hardness. The distribution of the strains in the blocks, on the other hand, is significantly more homogeneous, represented appropriately by the fitted normal distributions. For the lowest RA volume fraction of 8%, maximum strains of just over 4% are reached, which is only a fraction of the maximum strains found in the thin RA films.

In summary, a computational 3D micromechanical modeling approach is successfully employed to explore the influence of thin-film RA volume fraction on the local stress and strain distribution. The thin-film RA is explicitly embedded in the complex lath martensite structure for the first time. Key findings include:

- With diminishing RA volume fraction, both stress and in particular strain heterogeneity rises in the austenite films upon tensile loading.
- In the block-like lath martensite, stress and strain heterogeneity also tends to rise with descending RA volume fraction. Compared to the softer austenite films, the stress heterogeneity in the harder martensite blocks is more pronounced, while the strain heterogeneity is significantly less distinct.
- The martensite blocks slide visibly on the thin RA films, creating stress concentration and strain localization at the adjacent boundaries (grains, packets or blocks).

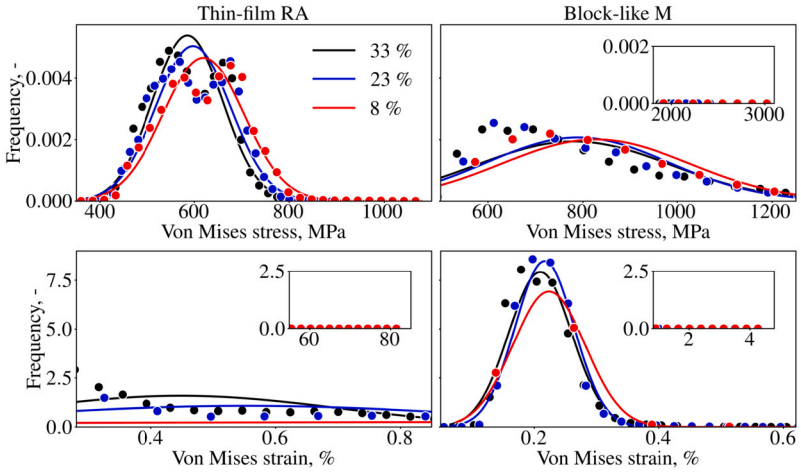

Fig. 4. Predicted equivalent stress (*top*) and strain distributions (*bottom*) at 0.3% macroscopic deformation as a function of thin-film retained austenite (RA) volume fraction. To emphasize the data trends of RA (*left*) and lath martensite (M) with its blocky morphology (*right*), normal distribution functions (solid lines) are fitted to the computed statistics (dots). The three inserts placed in the corners magnify the right-hand distribution tails.

CRediT authorship contribution statement

Tim Fischer: Writing – original draft, Visualization, Validation, Software, Methodology, Investigation, Formal analysis, Conceptualization. **Mina Amiri:** Writing – review & editing, Visualization, Validation, Software, Methodology, Investigation, Formal analysis, Conceptualization. **Joshua Kumpati:** Writing – review & editing, Visualization, Validation, Software, Methodology, Investigation, Formal analysis, Conceptualization. **Peter Hedström:** Writing – review & editing, Supervision, Resources, Project administration, Methodology, Funding acquisition, Conceptualization. **Annika Borgenstam:** Writing – review & editing, Supervision, Resources, Project administration, Methodology, Funding acquisition, Conceptualization.

Declaration of competing interest

The authors declare that they have no known competing financial interests or personal relationships that could have appeared to influence the work reported in this paper.

Acknowledgements

This research was conducted at the Center for Mechanics and Materials Design (www.mmd.center.kth.se). It is funded by industry partners, with a small counterpart funding from KTH Royal Institute of Technology. The authors would like to thank both parties for this. Computations were enabled by resources provided by the National Academic Infrastructure for Supercomputing in Sweden (NAISS) at KTH Royal Institute of Technology partially funded by the Swedish Research Council through grant agreement no. 2022-06725.

Data availability

The raw/processed data required to reproduce these findings cannot be shared at this time due to legal or ethical reasons.

References

[1] T.W.J. Kwok, D. Dye, A review of the processing, microstructure and property relationships in medium mn steels, Int. Mater. Rev. 68 (8) (2023) 1098–1134, https://doi.org/10.1080/09506608.2023.2199617.

[2] B. Sun, A.K. da Silva, Y. Wu, Y. Ma, H. Chen, C. Scott, D. Ponge, D. Raabe, Physical metallurgy of medium-mn advanced high-strength steels, Int. Mater. Rev. 68 (7) (2023) 786–824, https://doi.org/10.1080/09506608.2022.2153220.

[3] J. Kumpati, S.M. Hasan, M.B. Rolland, A. Borgenstam, Deconstructing the retained austenite stability: a comparative study of two-phase and bulk microstructures, Metall. Mater. Trans. A 55 (2024) 466–476, https://doi.org/10.1007/s11661-023-07258-8.

[4] S. Liu, Z. Xiong, H. Guo, C. Shang, R. Misra, The significance of multi-step partitioning: processing-structure-property relationship in governing high strength-high ductility combination in medium-manganese steels, Acta Mater. 124 (2017) 159–172, https://doi.org/10.1016/j.actamat.2016.10.067.

[5] S. Morito, H. Tanaka, R. Konishi, T. Furuhara, T. Maki, The morphology and crystallography of lath martensite in Fe-C alloys, Acta Mater. 51 (6) (2003) 1789–1799, https://doi.org/10.1016/S1359-6454(02)00577-3.

[6] S. Morito, H. Yoshida, T. Maki, X. Huang, Effect of block size on the strength of lath martensite in low carbon steels, Mater. Sci. Eng. A 438–440 (2006) 237–240, https://doi.org/10.1016/j.msea.2005.12.048.

[7] A. Shibata, T. Nagoshi, M. Sone, S. Morito, Y. Higo, Evaluation of the block boundary and sub-block boundary strengths of ferrous lath martensite using a micro-bending test, Mater. Sci. Eng. A 527 (29) (2010) 7538–7544, https://doi.org/10.1016/j.msea.2010.08.026.

[8] S. Morito, X. Huang, T. Furuhara, T. Maki, N. Hansen, The morphology and crystallography of lath martensite in alloy steels, Acta Mater. 54 (19) (2006) 5323–5331, https://doi.org/10.1016/j.actamat.2006.07.009.

[9] K. Kwak, Y. Mine, S. Morito, T. Ohmura, K. Takashima, Correlation between strength and hardness for substructures of lath martensite in low- and medium-carbon steels, Mater. Sci. Eng. A 856 (2022) 144007, https://doi.org/10.1016/j.msea.2022.144007.

[10] A. Shibata, G. Miyamoto, S. Morito, A. Nakamura, T. Moronaga, H. Kitano, I. Gutierrez-Urrutia, T. Hara, K. Tsuzaki, Substructure and crystallography of lath martensite in as-quenched interstitial-free steel and low-carbon steel, Acta Mater. 246 (2023) 118675, https://doi.org/10.1016/j.actamat.2023.118675.

[11] S. Morito, Y. Edamatsu, K. Ichinotani, T. Ohba, T. Hayashi, Y. Adachi, T. Furuhara, G. Miyamoto, N. Takayama, Quantitative analysis of three-dimensional morphology of martensite packets and blocks in iron-carbon-manganese steels, J. Alloys Compd. 577 (2013) S587–S592, https://doi.org/10.1016/j.jallcom.2012.02.004.

[12] E. Galindo-Nava, P.R.-D. del Castillo, A model for the microstructure behaviour and strength evolution in lath martensite, Acta Mater. 98 (2015) 81–93, https://doi.org/10.1016/j.actamat.2015.07.018.

[13] B. Hutchinson, P. Bate, D. Lindell, A. Malik, M. Barnett, P. Lynch, Plastic yielding in lath martensites – an alternative viewpoint, Acta Mater. 152 (2018) 239–247, https://doi.org/10.1016/j.actamat.2018.04.039.

[14] L. Morsdorf, O. Jeannin, D. Barbier, M. Mitsuhara, D. Raabe, C. Tasan, Multiple mechanisms of lath martensite plasticity, Acta Mater. 121 (2016) 202–214, https://doi.org/10.1016/j.actamat.2016.09.006.

[15] L. Morsdorf, C. Tasan, D. Ponge, D. Raabe, 3d structural and atomic-scale analysis of lath martensite: effect of the transformation sequence, Acta Mater. 95 (2015) 366–377, https://doi.org/10.1016/j.actamat.2015.05.023.

[16] A. Stormvinter, G. Miyamoto, T. Furuhara, P. Hedström, A. Borgenstam, Effect of carbon content on variant pairing of martensite in Fe–C alloys, Acta Mater. 60 (20) (2012) 7265–7274, https://doi.org/10.1016/j.actamat.2012.09.046.

[17] G. Miyamoto, N. Takayama, T. Furuhara, Accurate measurement of the orientation relationship of lath martensite and bainite by electron backscatter diffraction analysis, Scr. Mater. 60 (12) (2009) 1113–1116, https://doi.org/10.1016/j.scriptamat.2009.02.053.

[18] B. Sandvik, C. Wayman, Characteristics of lath martensite: part II. Crystallographic and substructural features, Metall. Trans. A 14 (4) (1983) 809–822, https://doi.org/10.1007/BF02644284.

[19] B. Sandvik, C. Wayman, Characteristics of lath martensite: part II. The martensite-austenite interface, Metall. Trans. A 14 (4) (1983) 823–834, https://doi.org/10.1007/BF02644285.
[20] T. Moritani, N. Miyajima, T. Furuhara, T. Maki, Comparison of interphase boundary structure between bainite and martensite in steel, Scr. Mater. 47 (3) (2002) 193–199, https://doi.org/10.1016/S1359-6462(02)00128-8.
[21] S. He, B. He, K. Zhu, R. Ding, H. Chen, M. Huang, Revealing the role of dislocations on the stability of retained austenite in a tempered bainite, Scr. Mater. 168 (2019) 23–27, https://doi.org/10.1016/j.scriptamat.2019.04.019.
[22] X. Xiong, B. Chen, M. Huang, J. Wang, L. Wang, The effect of morphology on the stability of retained austenite in a quenched and partitioned steel, Scr. Mater. 68 (5) (2013) 321–324, https://doi.org/10.1016/j.scriptamat.2012.11.003.
[23] D. Raabe, B. Sun, A. Kwiatkowski Da Silva, B. Gault, H.-W. Yen, K. Sedighiani, P. Thoudden Sukumar, I.R. Souza Filho, S. Katnagallu, E. Jägle, P. Kürnsteiner, N. Kusampudi, L. Stephenson, M. Herbig, C.H. Liebscher, H. Springer, S. Zaefferer, V. Shah, S.-L. Wong, C. Baron, M. Diehl, F. Roters, D. Ponge, Current challenges and opportunities in microstructure-related properties of advanced high-strength steels, Metall. Mater. Trans. A 51 (2020) 5517–5586, https://doi.org/10.1007/s11661-020-05947-2.
[24] A.-P. Pierman, O. Bouaziz, T. Pardoen, P. Jacques, L. Brassart, The influence of microstructure and composition on the plastic behaviour of dual-phase steels, Acta Mater. 73 (2014) 298–311, https://doi.org/10.1016/j.actamat.2014.04.015.
[25] K. Ismail, A. Perlade, P.J. Jacques, T. Pardoen, L. Brassart, Impact of second phase morphology and orientation on the plastic behavior of dual-phase steels, Int. J. Plast. 118 (2019) 130–146, https://doi.org/10.1016/j.ijplas.2019.02.005.
[26] Q. Lai, L. Brassart, O. Bouaziz, M. Gouné, M. Verdier, G. Parry, A. Perlade, Y. Bréchet, T. Pardoen, Influence of martensite volume fraction and hardness on the plastic behavior of dual-phase steels: experiments and micromechanical modeling, Int. J. Plast. 80 (2016) 187–203, https://doi.org/10.1016/j.ijplas.2015.09.006.
[27] F. Maresca, V. Kouznetsova, M. Geers, Deformation behaviour of lath martensite in multi-phase steels, Scr. Mater. 110 (2016) 74–77, https://doi.org/10.1016/j.scriptamat.2015.08.004.
[28] L. Liu, F. Maresca, J. Hoefnagels, T. Vermeij, M. Geers, V. Kouznetsova, Revisiting the martensite/ferrite interface damage initiation mechanism: the key role of substructure boundary sliding, Acta Mater. 205 (2021) 116533, https://doi.org/10.1016/j.actamat.2020.116533.
[29] L. Liu, F. Maresca, J. Hoefnagels, M. Geers, V. Kouznetsova, A multi-scale framework to predict damage initiation at martensite/ferrite interface, J. Mech. Phys. Solids 168 (2022) 105018, https://doi.org/10.1016/j.jmps.2022.105018.
[30] L. Liu, F. Maresca, T. Vermeij, J. Hoefnagels, M. Geers, V. Kouznetsova, An integrated experimental-numerical study of martensite/ferrite interface damage initiation in dual-phase steels, Scr. Mater. 239 (2024) 115798, https://doi.org/10.1016/j.scriptamat.2023.115798.
[31] F. Maresca, V. Kouznetsova, M. Geers, Subgrain lath martensite mechanics: a numerical–experimental analysis, J. Mech. Phys. Solids 73 (2014) 69–83, https://doi.org/10.1016/j.jmps.2014.09.002.
[32] F. Maresca, V.G. Kouznetsova, M.G.D. Geers, On the role of interlath retained austenite in the deformation of lath martensite, Model. Simul. Mater. Sci. Eng. 22 (4) (2014) 045011.
[33] C. Tasan, M. Diehl, D. Yan, C. Zambaldi, P. Shanthraj, F. Roters, D. Raabe, Integrated experimental–simulation analysis of stress and strain partitioning in multiphase alloys, Acta Mater. 81 (2014) 386–400, https://doi.org/10.1016/j.actamat.2014.07.071.
[34] F. Briffod, T. Shiraiwa, K. Yamazaki, M. Enoki, Integrated experimental–numerical investigation of strain partitioning and damage initiation in a low-carbon lath martensitic steel, Mater. Sci. Eng. A 876 (2023) 145148, https://doi.org/10.1016/j.msea.2023.145148.
[35] F. Briffod, H. Hu, T. Shiraiwa, M. Enoki, Effect of in-lath slip strength on the strain partitioning in a dual-phase steel investigated by high-resolution digital image correlation and crystal plasticity simulations, Mater. Sci. Eng. A 862 (2023) 144413, https://doi.org/10.1016/j.msea.2022.144413.
[36] F. Bachmann, R. Hielscher, H. Schaeben, Texture analysis with MTEX – free and open source software toolbox, in: Texture and Anisotropy of Polycrystals III, in: Solid State Phenomena, vol. 160, Trans Tech Publications Ltd, 2010, pp. 63–68.
[37] F. Niessen, T. Nyyssönen, A.A. Gazder, R. Hielscher, Parent grain reconstruction from partially or fully transformed microstructures in MTEX, J. Appl. Crystallogr. 55 (1) (2022) 180–194, https://doi.org/10.1107/S1600576721011560.
[38] R. Hielscher, T. Nyyssönen, F. Niessen, A.A. Gazder, The variant graph approach to improved parent grain reconstruction, Materialia 22 (2022) 101399, https://doi.org/10.1016/j.mtla.2022.101399.
[39] G. Kurdjumow, G. Sachs, Über den Mechanismus der Stahlhärtung, Z. Phys. 64 (5) (1930) 325–343, https://doi.org/10.1007/BF01397346.
[40] Z. Nishiyama, X-ray investigation of the mechanism of the transformation from face-centred cubic lattice to body-centred cubic, Science Reports Tohoku University, Tohoku University, Japan, 1934, p. 637.
[41] A.B. Greninger, A.R. Troiano, The mechanisms of martensite formation, JOM 1 (1949) 590–598.
[42] F. Roters, M. Diehl, P. Shanthraj, P. Eisenlohr, C. Reuber, S. Wong, T. Maiti, A. Ebrahimi, T. Hochrainer, H.-O. Fabritius, S. Nikolov, M. Friák, N. Fujita, N. Grilli, K. Janssens, N. Jia, P. Kok, D. Ma, F. Meier, E. Werner, M. Stricker, D. Weygand, D. Raabe, Damask – the Düsseldorf advanced material simulation kit for modeling multi-physics crystal plasticity, thermal, and damage phenomena from the single crystal up to the component scale, Comput. Mater. Sci. 158 (2019) 420–478, https://doi.org/10.1016/j.commatsci.2018.04.030.
[43] F. Sun, E.D. Meade, N.P. O'Dowd, Strain gradient crystal plasticity modelling of size effects in a hierarchical martensitic steel using the Voronoi tessellation method, Int. J. Plast. 119 (2019) 215–229, https://doi.org/10.1016/j.ijplas.2019.03.009.
[44] J. Park, K. Lee, J.-H. Kang, J.-Y. Kang, S. Hong, S. Kwon, M.-G. Lee, Hierarchical microstructure based crystal plasticity-continuum damage mechanics approach: model development and validation of rolling contact fatigue behavior, Int. J. Plast. 143 (2021) 103025, https://doi.org/10.1016/j.ijplas.2021.103025.
[45] T. Fischer, T. Zhou, C.F. Dahlberg, P. Hedström, Relating stress/strain heterogeneity to lath martensite strength by experiments and dislocation density-based crystal plasticity, Int. J. Plast. 174 (2024) 103917, https://doi.org/10.1016/j.ijplas.2024.103917.
[46] C. Du, J. Hoefnagels, R. Vaes, M. Geers, Block and sub-block boundary strengthening in lath martensite, Scr. Mater. 116 (2016) 117–121, https://doi.org/10.1016/j.scriptamat.2016.01.043.
[47] T. Fischer, C.F. Dahlberg, P. Hedström, Sensitivity of local cyclic deformation in lath martensite to flow rule and slip system in crystal plasticity, Comput. Mater. Sci. 222 (2023) 112106, https://doi.org/10.1016/j.commatsci.2023.112106.
[48] R. Quey, L. Renversade, Optimal polyhedral description of 3D polycrystals: method and application to statistical and synchrotron X-ray diffraction data, Comput. Methods Appl. Mech. Eng. 330 (2018) 308–333, https://doi.org/10.1016/j.cma.2017.10.029.
[49] E. Schmid, W. Boas, Kristallplastizität – Mit besonderer Berücksichtigung der Metalle, vol. 17, Springer-Verlag, Berlin Heidelberg, 1935.
[50] J. Hutchinson, Bounds and self-consistent estimates for creep of polycrystalline materials, Proc. R. Soc. A, Math. Phys. Eng. Sci. 348 (1652) (1976) 101–127.
[51] D. Peirce, R. Asaro, A. Needleman, Material rate dependence and localized deformation in crystalline solids, Acta Metall. 31 (12) (1983) 1951–1976, https://doi.org/10.1016/0001-6160(83)90014-7.
[52] S.R. Kalidindi, Incorporation of deformation twinning in crystal plasticity models, J. Mech. Phys. Solids 46 (2) (1998) 267–290, https://doi.org/10.1016/S0022-5096(97)00051-3.
[53] Y. Mine, K. Hirashita, H. Takashima, M. Matsuda, K. Takashima, Micro-tension behaviour of lath martensite structures of carbon steel, Mater. Sci. Eng. A 560 (2013) 535–544, https://doi.org/10.1016/j.msea.2012.09.099.
[54] J.S. Nagra, A. Brahme, R.A. Lebensohn, K. Inal, Efficient fast Fourier transform-based numerical implementation to simulate large strain behavior of polycrystalline materials, Int. J. Plast. 98 (2017) 65–82, https://doi.org/10.1016/j.ijplas.2017.07.001.
[55] L. van Wees, A. Singh, M. Obstalecki, P. Shade, T. Turner, M. Kasemer, An assessment of polarized light microscopy as a characterization method for crystal plasticity simulations, Materialia 31 (2023) 101872, https://doi.org/10.1016/j.mtla.2023.101872.
[56] D.C. Pagan, C.R. Pash, A.R. Benson, M.P. Kasemer, Graph neural network modeling of grain-scale anisotropic elastic behavior using simulated and measured microscale data, npj Comput. Mater. 8 (2022) 259, https://doi.org/10.1038/s41524-022-00952-y.